PHYSICAL REVIEW B **93**, 140409(R) (2016)

Identifying multiexcitons in MoS_2 monolayers at room temperature

Hyun Seok Lee,[1,*] Min Su Kim,[1] Hyun Kim,[1,2] and Young Hee Lee[1,2,3,†]

[1]*Center for Integrated Nanostructure Physics (CINAP), Institute for Basic Science (IBS), Sungkyunkwan University, Suwon 440-746, Korea*

[2]*Department of Energy Science, Sungkyunkwan University, Suwon 440-746, Korea*

[3]*Department of Physics, Sungkyunkwan University, Suwon 440-746, Korea*

(Received 12 October 2015; published 19 April 2016)

One of the unique features of atomically thin two-dimensional materials is strong Coulomb interactions due to the reduced dielectric screening effect; this feature enables the study of many-body phenomena such as excitons, trions, and biexcitons. However, identification of biexcitons remains unresolved owing to their broad peak feature at room temperature. Here, we investigate multiexcitons in monolayer MoS_2 using both electrical and optical doping and identify the transition energies for each exciton. The binding energy of the assigned biexciton is twice that of the trion, in quantitative agreement with theoretical predictions. The biexciton population is predominant under optical doping but negligible under electrical doping. The biexciton population is quadratically proportional to the exciton population, obeying the mass-action theory. Our results illustrate the stable formation of not only trions but also biexcitons due to strong Coulomb interaction even at room temperature; therefore, these results provide a deeper understanding of the complex excitonic behaviors in two-dimensional semiconductors.

DOI: 10.1103/PhysRevB.93.140409

Monolayer transition-metal dichalcogenides (TMDs) have been highlighted as a promising platform for fundamental studies of many-body interactions because the interaction emerges strongly even at room temperature because of reduced dielectric screening [1–18]. Exciton binding energies are typically large in two-dimensional (2D) systems because of the strong Coulomb interactions between charged particles; they generally range from 0.3 to 1.0 eV, and those of higher-order excitons range from 18 to 70 meV [19,20]. These binding energies are still sufficient for distinguishing higher-order excitons at room temperature, whereas they have rarely been realized in three-dimensional semiconductors or quantum wells (QWs) because of their relatively small binding energies. The tightly bound electron-hole pairs in TMDs allow negatively charged trions to be generated by electrostatic doping [4], triggering research on exciton complexes, including biexcitons, in various TMDs [5,20–25]. This unique feature of 2D semiconductors provides the opportunity to elucidate new optoelectronic phenomena involving many-body interactions that can be applied to a new class of quantum emitters for light-emitting diodes [26], optical communication devices [27], and monolayer lasers [28]; thus, it is necessary to understand these many-body interactions for practical applications realized by manipulating excitons precisely, as well as the fundamental physics of new emergent 2D systems.

However, one fundamental question is why biexcitons are not identified at room temperature, whereas trions are commonly reported [4,6,7,9,25]. In conventional semiconductors, including bulk materials, quantum dots, and QWs, biexciton formation at room temperature has been reported [29–31]. Although the biexciton binding energy (∼30 meV) of CdSe QWs is much lower than that of TMDs (which exceeds ∼60 meV) [19,20], biexcitons form stably even at room temperature, because the binding energy is higher than the thermal energy, $k_BT = 26$ meV, where k_B and T are the Boltzmann constant and room temperature, respectively [29]. Even though biexcitons have a stronger binding energy than trions in TMDs, biexcitons have rarely been reported at room temperature except for a report on biexciton observation at edges and grain boundaries of WS_2 monolayer flakes [32], while they are well studied in low-temperature experiments as well as theoretically [21,25,33].

The transition energies of the exciton and trion in monolayer MoS_2, a representative TMD, have been extensively investigated. Figure 1(a) summarizes the reported data from photoluminescence (PL) experiments on MoS_2 monolayers at room temperature [1–18]. The inset shows selected data obtained using SiO_2/Si substrates [2,4,5,7–9,12–15,18]. The observed A-peak positions are scattered in a wide energy range from 1.90 to 1.83 eV. The peaks assigned to the neutral exciton (A^X, solid circles) and trion (A^T, open circles) in the A exciton mode fluctuate greatly, even overlapping each other. This A peak was further obscured by the large unassigned values (A, stars), for which the fluctuation ($\Delta E \approx 70$ meV) exceeds the theoretical predictions and experimental determinations of not only the trion binding energy (∼30 meV) [19,24,34], but also the biexciton binding energy (>60 meV) [19,20,33]. This large deviation of the peak position further exemplifies the ambiguity of distinguishing exciton and trion peaks from each other owing to broad features of excitonic peaks in MoS_2 monolayers even at low temperature [35], while sharp and isolated peaks of multiexcitons were observed in other TMDs [21,25]. Moreover, this disagreement of the peak position is more prominently affected by complex exciton generation depending on the excitation laser intensity [36], rather than by the sample conditions arising from different sampling processes. The changes in the binding energy of excitons and trions depending on the doping state, defects, growth methods, and dielectric substrates are not sufficient to cover the large deviation under the same measurement conditions, whereas the populations are noticeably affected [5,9,12,18].

In this regard, we speculate that the reported data [Fig. 1(a)] may include biexcitons, because their binding energy is within

*hs.lee@skku.edu

†leeyoung@skku.edu

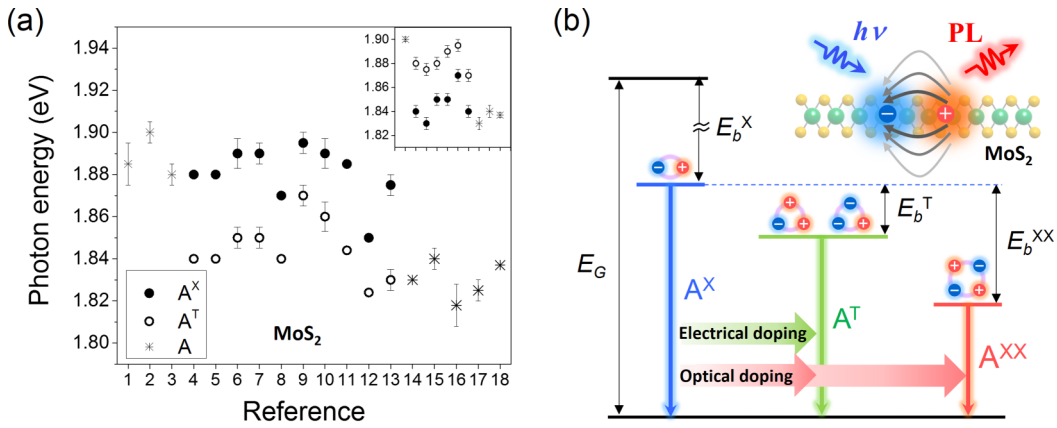

FIG. 1. (a) Assigned peak positions of A^X (solid circles), A^T (open circles), and unassigned A (stars) plotted from various references for PL measurement in MoS_2 monolayers at room temperature. Inset: Selected data obtained using SiO_2/Si substrates. (b) Definition of binding energies (E_b^X, E_b^T, and E_b^{XX}) and transition energies (A^X, A^T, and A^{XX}) for exciton, trion, and biexciton, respectively.

ΔE. The positions of excitons and trions were not clearly identified with a general consensus [Fig. 1(a)], and no effort was made to distinguish possible biexcitons from broad peaks, although the peak positions should be identified by systematic control of the doping levels of samples and the excitation laser power, because biexcitons are formed at high exciton densities [21], and neutral excitons are generated at extremely low excitation power [36], whereas trions are rarely observed at weak optical densities [2].

Here, we identify multiexcitons by measuring the PL of monolayer MoS_2 under systematic modulations of the electrostatic doping states and exciting optical density at room temperature. Figure 1(b) schematically depicts the binding energies (E_b^X, E_b^T, and E_b^{XX}) and transition energies (A^X, A^T, and A^{XX}) for the neutral exciton, trion, and biexciton in the A exciton mode, respectively, where $E_b^X = E_G - A^X$, $E_b^T = A^X - A^T$, $E_b^{XX} = A^X - A^{XX}$, and E_G denotes the band gap [6,21,22,37–39]. As the photocarrier density, which is modulated by the excitation laser power (P_{ex}) to realize optical doping (OD), and the intrinsic carrier density, which is controlled by electrical doping (ED), increase, A^X are converted into positive or negative A^T, depending on the excess carrier type. As the population of electron-hole pairs increases in proportion to the OD, excitons are accordingly converted into A^{XX}.

To investigate the multiexcitons depending on ED and OD, we used monolayer MoS_2 field-effect transistors (FETs), where monolayer MoS_2 flakes were synthesized by chemical vapor deposition [40]. The intrinsic doping states are estimated by electrical characterization, because MoS_2 reveals intrinsic n doping arising from inherent impurities, defects, and substrate effects [4,6,7,44]. Figure 2(a) shows the drain current (I_D) for $V_D = 0.1$ V as a function of V_G. The presence of a threshold V_G near -20 V clearly indicates the n doping at $V_G = 0$ V, whereas slight p doping is observed at $V_G < -40$ V, where we defined the neutral doping state as $V_{G0} = -35$ V [45]. The Fermi level shift ($\Delta\mu = \mu - \mu_0$) was calculated from the back-gate capacitance and displayed on the right-hand axis of Fig. 2(a), where μ is the Fermi level and μ_0 is μ for $V_G = -35$ V (see Supplemental Material [46]).

The PL was measured at various P_{ex} values for OD using a diode laser with a wavelength of 405 nm and an objective lens with a numerical aperture of 0.6 [49], where the ED density was modulated by V_G in the range from -70 to 70 V for each P_{ex}. For $P_{ex} = 0.5 - 500\,\mu$W, corresponding photocarrier generation rates are estimated from $\sim 5.5 \times 10^{18}$ to $\sim 5.5 \times 10^{21}$ cm^{-2} s^{-1}. Figure 2(b) shows the P_{ex}-dependent PL spectra at $V_G = -40$ V for the nearly neutral state. In the low-power range ($0.5-5\,\mu$W), a sharp peak ($P_0 \approx 1.9$ eV) with a nearly symmetric shape is generated. A new inflection point ($P_1 \approx 1.87$ eV) emerges at $10-500\,\mu$W. At 500 μW, another new inflection point ($P_2 \approx 1.84$ eV) is prominent. The inset shows the full width at half maximum (FWHM) curve for the spectra, which has an S shape. As P_{ex} increases, the FWHM slowly varies and rapidly increases to saturate at the high-power limit, which is consistent with the new emergence of the P_1 and P_2 peaks rather than just a simple P_0 peak shift. This behavior agrees well with the biexciton emergence in QWs at room temperature [29].

Figures 2(c) and 2(d) show the measured and intensity-normalized PL spectra, respectively, for three typical P_{ex} values as a function of V_G. At $P_{ex} = 0.5\,\mu$W [Fig. 2(c), top], the P_0 intensity decreases in response to V_G, while the peak position is not changed [Fig. 2(d), top, black-dashed circle]. These results agree well with the previous report, in which we identify $P_0 = A^X$ [2]. Exciton saturation with increasing electron density is attributed to Pauli blocking effects resulting from the presence of excess free electrons supplied by ED [2,24]. Laser illumination with energy exceeding the exciton transition energies excites electron-hole pairs, which are further thermalized to the lowest exciton energy level. Under high electron doping, the occupied states block the injection of photoexcited electrons into the states and consequently exciton emission is reduced. Additionally, a Coulomb screening effect due to electron plasma may play a role for E_b^X modulation [24] but this effect is negligible because of the strong binding effects, which is confirmed by the experimental result that the peak position is not altered in this doping range [Fig. 2(d), top], in good agreement with other experimental results [2].

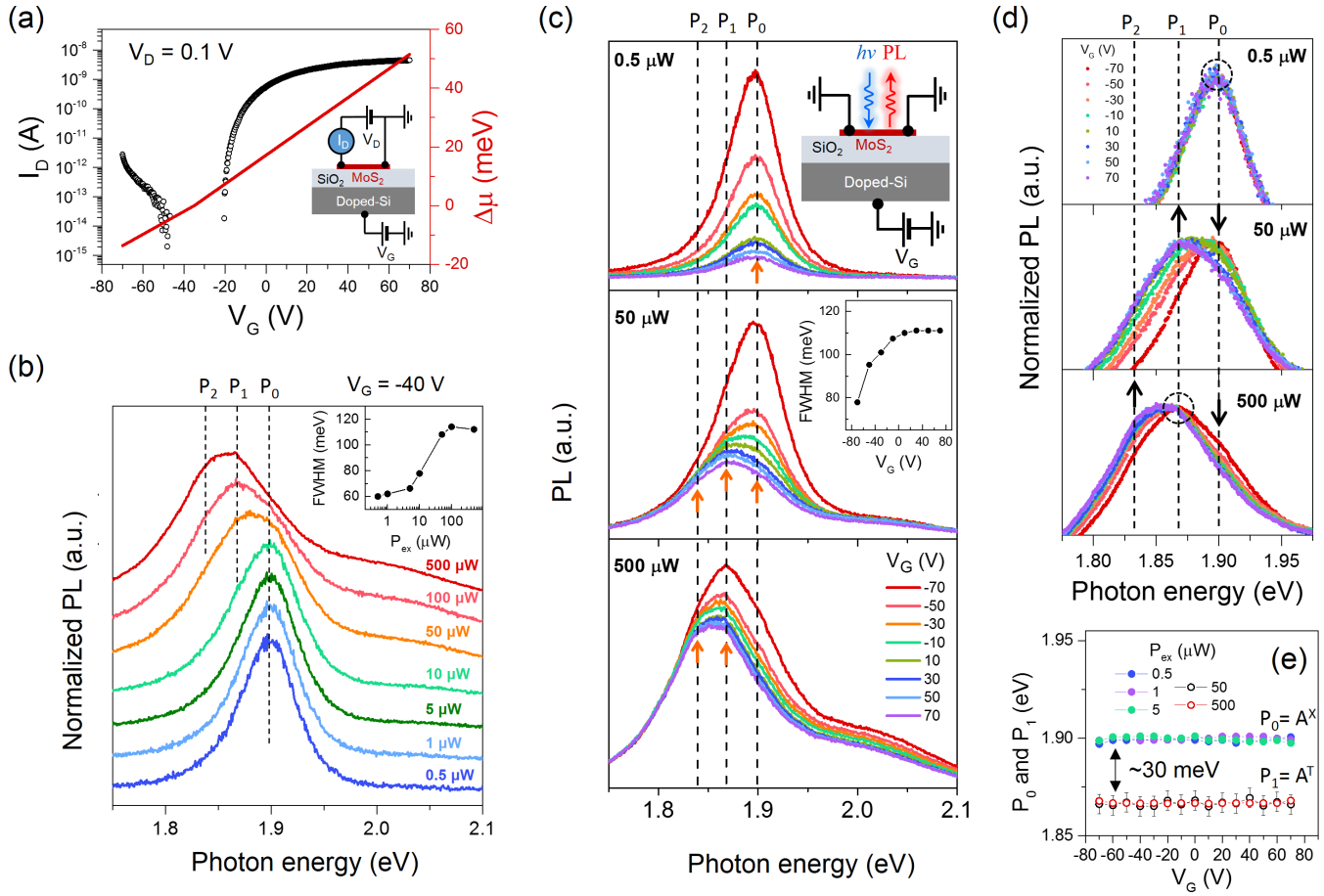

FIG. 2. (a) Transfer characteristics of drain current (I_D) for a drain voltage (V_D) of 0.1 V and calculated Fermi level shift as a function of V_G. Inset: Schematic of electrical characterization of the FET. (b) PL spectra as a function of P_{ex} at $V_G = -40$ V. (c) PL spectra as a function of V_G at $P_{ex} = 0.5$, 50, and 500 μW. Orange arrows indicate the inflection points of PL spectra corresponding to dashed lines for P_0, P_1, and P_2. Inset: FWHM as a function of V_G at $P_{ex} = 50\,\mu$W. (d) Normalized PL spectra for (c). Dashed black circle: unchanged inflection. (e) Peak positions as a function of V_G for P_0 and P_1 at various P_{ex}.

At $P_{ex} = 50\,\mu$W [Fig. 2(c), middle], the P_1 peak is more prominent as the electron doping density increases, whereas the P_0 population is drastically reduced. The FWHM gradually grows and saturates at high V_G (inset), implying the emergence of a new peak, not a peak shift. These behaviors are clearly visible in Fig. 2(d), middle, and agree with previous reports on trions [4,13]. Therefore, we identify P_1 as A^T. The reported E_b^T agrees quantitatively with our experimental results ($P_0 - P_1 \approx 30$ meV) [19,20,24]. At $P_{ex} = 500\,\mu$W [Fig. 2(c), bottom], the emergence of the P_2 peak is clearly visible in heavily n-doped states. Further, the P_1 intensity is modulated, but the inflection point suggests the P_1 position is not altered with the doping [Fig. 2(d), bottom, black-dashed circle]. Figure 2(e) shows the peak positions of P_0 (A^X) and P_1 ($= A^T$) as a function of V_G for various P_{ex}. The changes in the peak position depending on the doping state for A^X and A^T are negligible, in agreement with results for $MoSe_2$ and $MoTe_2$ [22,23]. This doping independence of A^X and A^T positions is contrasted to a 2D electron gas (2DEG) of QWs [50,51]. The 2DEG is easily degenerate by doping, $A^X - A^T = E^T + E_F$ and $E_F = \mu - E_C > 0$, where E_F, μ, and E_C are defined as the Fermi energy, Fermi level, and conduction band, respectively. E^T is defined as the energy to dissociate one electron from two bound electrons of a trion up to E_C. Note that in our definition, $A^X - A^T = E_b^T$, and E_b^T is an energy to dissociate a trion into one exciton and one free electron, which is slightly different from the heavily degenerated 2DEGs, where the Fermi level (μ) in MoS_2 is located within the band gap. Thus, E_F does not play a role in our definition. In our experimental conditions of P_{ex} up to $\sim$500 μW, no appreciable A^T shift was observed. Nevertheless, at higher P_{ex}, strong plasma screening effects may occur, altering the exciton peak shift. Additionally, the E_b^T values of TMDs have generally been studied at low temperature. At room temperature, the peaks for exciton complexes are broadened and the peak positions are redshifted by thermal effects, but the E_b^T values are similar to those at low temperature, confirming our analysis [22,24].

As discussed in Fig. 2(b), the emergence of the new peak P_2 is obvious at high powers (50–500 μW). The FWHM increases gradually with the generation of A^T in the intermediate power range [Fig. 2(b), inset]. The rapid increase in the FWHM and saturation at high powers is another indication of P_2 peak emergence. At 500 μW in Fig. 2(c), the P_2 intensity does not change appreciably with V_G modulation, whereas the A^T peak intensity is modulated significantly. The strong dependence of the P_2 peak on P_{ex} and its position below

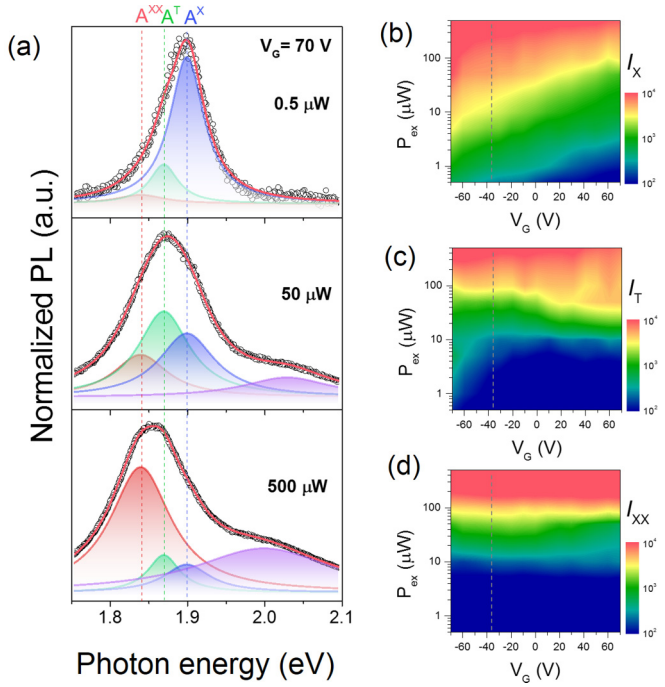

FIG. 3. (a) PL spectra at $V_G = 70\,\mathrm{V}$ for $P_{ex} = 0.5$, 50, and 500 μW and their Lorentzian deconvolutions for $P_0 = A^X$, $P_1 = A^T, P_2 = A^{XX}$. Log-scale intensity contours for (b) I_X (for A^X), (c) I_T (for A^T), and (d) I_{XX} (for A^{XX}) as functions of P_{ex} and V_G derived from the deconvolution results in (a). Dashed line indicates $V_{G0} = -35\,\mathrm{V}$.

A^T are biexcitonic features [21,29]. From the observed peak position of P_2 (~1.84 eV), $E_b^{XX} = P_0 - P_2 \approx 60$ meV and $P_2 = A^{XX}$. Together with the observed $E_b^T \approx 30$ meV, our result is in excellent agreement with theoretical predictions of the biexciton binding energy, $E_b^{XX}/E_b^T \approx 2$ [19,20,39].

To estimate the relative populations of multiexcitons, the PL spectra were deconvoluted into the fixed peak positions at various P_{ex} and V_G on the basis of the results that the positions and binding energies of A^X, A^T, and A^{XX} do not depend on P_{ex} and V_G. Figure 3(a) shows typical examples of the fitted results for n^+ doping ($V_G = 70\,\mathrm{V}$) at various P_{ex}. For all of the PL spectra, the A-peak deconvolution reveals three peaks. Overall, as P_{ex} increases, the A^{XX} and A^T peaks become more prominent, while the A^X peak diminishes. Figures 3(b)–3(d) show the log-scale population contours for each exciton, I_X (for A^X), I_T (for A^T), and I_{XX} (for A^{XX}), respectively, as functions of P_{ex} and V_G from the deconvolution results. For I_X [Fig. 3(b)], the carrier modulation by ED is less effective at high optical densities than at low optical densities, as the optically generated electron-hole plasma under high P_{ex} dominates the electrically modulated carriers, and the number of neutral excitons that are converted to multiexcitons is proportional to P_{ex}. Figure 3(c) shows that the positive I_T increases dramatically with p doping ($V_G < -35\,\mathrm{V}$) at low P_{ex} ($0.5-10\,\mu$W). Similarly, the negative I_T increases gradually with n doping ($V_G > -35\,\mathrm{V}$) in the intermediate P_{ex} range ($10-100\,\mu$W). In Fig. 3(d), however, the V_G dependence of I_{XX} is almost negligible except in the heavily n-doped region at intermediate P_{ex}, but the P_{ex} dependence of I_{XX} is prominent [21].

To confirm the identities of the newly assigned biexciton in this study, we characterized the modulation behavior of relative populations on the basis of the mass action law for biexcitons [52]. In a chemical equilibrium state at a given temperature, the biexciton can be identified by the quadratic relation between I_{XX} and I_X, $I_{XX} \propto I_X^\alpha$, where in ideal biexciton generation, the exponent α should be 2 [21,25,29,52]. Figure 4(a) shows log-log scale I_X-I_{XX} plots, where the linear slope corresponds to the exponent α. Note that in a high-population region ($P_{ex} \geqslant 10\,\mu$W), $\alpha \sim 2$ for all doping levels, which is typical evidence for identifying biexcitons [21,25,29,52]. Further, in a low-population region ($P_{ex} < 10\,\mu$W), $\alpha < 2$ owing to a deficiency of states in equilibrium, as is normally observed in QW systems and WSe_2 [21,52]. For a given I_{XX} and I_X for various V_G, ϕ is determined from the I_{XX} intercepts [Fig. 4(c), inset]. Because ϕ ($\propto I_{XX}/I_X^2$) is linearly proportional to V_G ($\propto n$), the relationship $I_{XX}/I_X^2 \propto n$ is valid.

This work was supported by IBS-R011-D1.

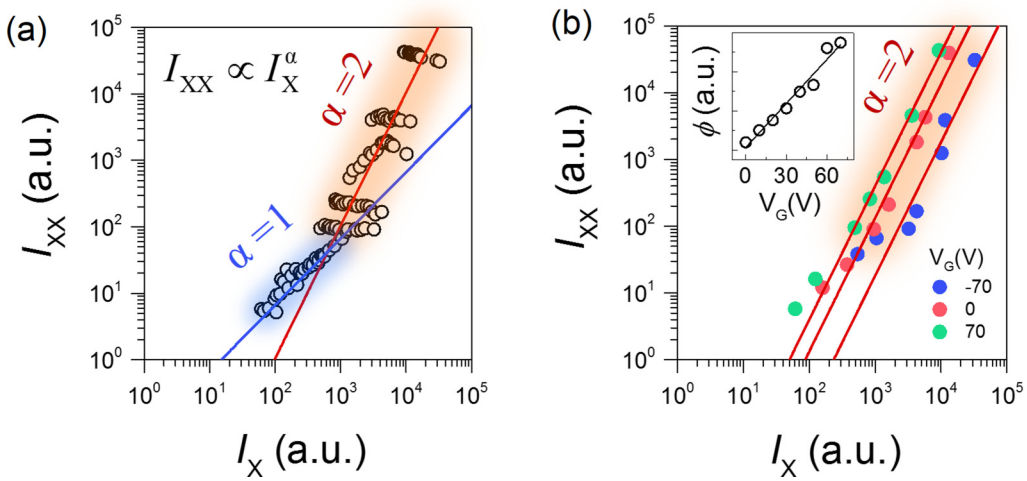

FIG. 4. (a) Log-log scale I_{XX}-I_X plots obeying the relationship $I_{XX} \propto I_X^\alpha$. Linear lines are fits for $\alpha = 1$ (blue) and 2 (red). (b) Log-log scale I_{XX}-I_X plots for $V_G = -70$, 0, and 70 V and their linear fits with $\alpha = 2$. Inset: I_{XX} intercept of square-law lines (ϕ) as a function of $V_G (\geqslant 0\,\mathrm{V})$.

[1] K. F. Mak, C. Lee, J. Hone, J. Shan, and T. F. Heinz, Phys. Rev. Lett. **105**, 136805 (2010).
[2] A. K. M. Newaz, D. Prasai, J. I. Ziegler, D. Caudel, S. Robinson, R. F. Haglund, and K. I. Bolotin, Solid State Commun. **155**, 49 (2013).
[3] D. Z. Sun, Y. Rao, G. A. Reider, G. G. Chen, Y. M. You, L. Brezin, A. R. Harutyunyan, and T. F. Heinz, Nano Lett. **14**, 5625 (2014).
[4] K. F. Mak, K. L. He, C. Lee, G. H. Lee, J. Hone, T. F. Heinz, and J. Shan, Nat. Mater. **12**, 207 (2013).
[5] S. Mouri, Y. Miyauchi, and K. Matsuda, Nano Lett. **13**, 5944 (2013).
[6] Y. X. Lin, X. Ling, L. L. Yu, S. X. Huang, A. L. Hsu, Y. H. Lee, J. Kong, M. S. Dresselhaus, and T. Palacios, Nano Lett. **14**, 5569 (2014).
[7] M. Buscema, G. A. Steele, H. S. J. van der Zant, and A. Castellanos-Gomez, Nano Res. **7**, 561 (2014).
[8] X. X. Wei, Z. H. Yu, F. R. Hu, Y. Cheng, L. W. Yu, X. Y. Wang, M. Xiao, J. Z. Wang, X. R. Wang, and Y. Shi, AIP Adv. **4**, 123004 (2014).
[9] H. Y. Nan, Z. L. Wang, W. H. Wang, Z. Liang, Y. Lu, Q. Chen, D. W. He, P. H. Tan, F. Miao, X. R. Wang, J. L. Wang, and Z. H. Ni, ACS Nano **8**, 5738 (2014).
[10] G. M. Akselrod, T. Ming, C. Argyropoulos, T. B. Hoang, Y. X. Lin, X. Ling, D. R. Smith, J. Kong, and M. H. Mikkelsen, Nano Lett. **15**, 3578 (2015).
[11] C. H. Lui, A. J. Frenzel, D. V. Pilon, Y. H. Lee, X. Ling, G. M. Akselrod, J. Kong, and N. Gedik, Phys. Rev. Lett. **113**, 166801 (2014).
[12] S. Wang, X. Wang, and J. H. Warner, ACS Nano **9**, 5246 (2015).
[13] J. Pei, J. Yang, R. Xu, Y.-H. Zeng, Y. W. Myint, S. Zhang, J.-C. Zheng, Q. Qin, X. Wang, W. Jiang, and Y. Lu, Small **11**, 6384 (2015).
[14] A. Splendiani, L. Sun, Y. B. Zhang, T. S. Li, J. Kim, C. Y. Chim, G. Galli, and F. Wang, Nano Lett. **10**, 1271 (2010).
[15] N. R. Kang, H. P. Paudel, M. N. Leuenberger, L. Tetard, and S. I. Khondaker, J. Phys. Chem. C **118**, 21258 (2014).
[16] A. Sobhani, A. Lauchner, S. Najmaei, C. Ayala-Orozco, F. F. Wen, J. Lou, and N. J. Halas, Appl. Phys. Lett. **104**, 031112 (2014).
[17] R. S. Sundaram, M. Engel, A. Lombardo, R. Krupke, A. C. Ferrari, P. Avouris, and M. Steiner, Nano Lett. **13**, 1416 (2013).
[18] J. Zhang, H. Yu, W. Chen, X. Tian, D. Liu, M. Cheng, G. Xie, W. Yang, R. Yang, X. Bai, D. Shi, and G. Zhang, ACS Nano **8**, 6024 (2014).
[19] A. Thilagam, J. Appl. Phys. **116**, 053523 (2014).
[20] D. K. Zhang, D. W. Kidd, and K. Varga, Nano Lett. **15**, 7002 (2015).
[21] Y. You, X.-X. Zhang, T. C. Berkelbach, M. S. Hybertsen, D. R. Reichman, and T. F. Heinz, Nat. Phys. **11**, 477 (2015).
[22] J. S. Ross, S. F. Wu, H. Y. Yu, N. J. Ghimire, A. M. Jones, G. Aivazian, J. Q. Yan, D. G. Mandrus, D. Xiao, W. Yao, and X. D. Xu, Nat. Commun. **4**, 1474 (2013).
[23] J. Yang, T. Lü, Y. W. Myint, J. Pei, D. Macdonald, J.-C. Zheng, and Y. Lu, ACS Nano **9**, 6603 (2015).
[24] C. J. Zhang, H. N. Wang, W. M. Chan, C. Manolatou, and F. Rana, Phys. Rev. B. **89**, 205436 (2014).
[25] J. Z. Shang, X. N. Shen, C. X. Cong, N. Peimyoo, B. C. Cao, M. Eginligil, and T. Yu, ACS Nano **9**, 647 (2015).
[26] F. Withers, O. Del Pozo-Zamudio, A. Mishchenko, A. P. Rooney, A. Gholinia, K. Watanabe, T. Taniguchi, S. J. Haigh, A. K. Geim, A. I. Tartakovskii, and K. S. Novoselov, Nat. Mater. **14**, 301 (2015).
[27] H. S. Lee, M. S. Kim, Y. Jin, G. H. Han, Y. H. Lee, and J. Kim, Adv. Opt. Mater. **3**, 943 (2015).
[28] S. F. Wu, S. Buckley, J. R. Schaibley, L. F. Feng, J. Q. Yan, D. G. Mandrus, F. Hatami, W. Yao, J. Vuckovic, A. Majumdar, and X. D. Xu, Nature (London) **520**, 69 (2015).
[29] J. Q. Grim, S. Christodoulou, F. Di Stasio, R. Krahne, R. Cingolani, L. Manna, and I. Moreels, Nat. Nanotechnol. **9**, 891 (2014).
[30] O. Fedorych, C. Kruse, A. Ruban, D. Hommel, G. Bacher, and T. Kummell, Appl. Phys. Lett. **100**, 061114 (2012).
[31] Y. Furutani, R. Kittaka, H. Miyake, K. Hiramatsu, and Y. Yamada, Appl. Phys. Express **5**, 072401 (2012).
[32] M. S. Kim, S. J. Yun, Y. Lee, C. Seo, G. H. Han, K. K. Kim, Y. H. Lee, and J. Kim, ACS Nano **10**, 2399 (2016).
[33] C. Mai, A. Barrette, Y. F. Yu, Y. G. Semenov, K. W. Kim, L. Y. Cao, and K. Gundogdu, Nano Lett. **14**, 202 (2014).
[34] T. C. Berkelbach, M. S. Hybertsen, and D. R. Reichman, Phys. Rev. B **88**, 045318 (2013).
[35] T. Kummell, W. Quitsch, S. Matthis, T. Litwin, and G. Bacher, Phys. Rev. B **91**, 125305 (2015).
[36] H. S. Lee, M. S. Kim, Y. Jin, G. H. Han, Y. H. Lee, and J. Kim, Phys. Rev. Lett. **115**, 226801 (2015).
[37] A. Ramasubramaniam, Phys. Rev. B **86**, 115409 (2012).
[38] K. L. He, N. Kumar, L. Zhao, Z. F. Wang, K. F. Mak, H. Zhao, and J. Shan, Phys. Rev. Lett. **113**, 026803 (2014).
[39] M. Z. Mayers, T. C. Berkelbach, M. S. Hybertsen, and D. R. Reichman, Phys. Rev. B **92**, 161404(R) (2015).
[40] Monolayer MoS_2 flakes were directly synthesized on a SiO_2 (300 nm)/Si substrate using a vapor phase reaction method [41]. Poly(methylmethacrylate) (950 K PMMA, MicroChem Corp., 4% chlorobenzene) was spin coated onto MoS_2 grown samples and dried under ambient conditions. The PMMA/MoS_2 layer was detached by soaking in a 1-M KOH solution for several minutes and was washed with de-ionized water. Finally, the PMMA/MoS_2 layer was transferred to the SiO_2 (300 nm)/Si wafer, and the PMMA was removed using acetone [11]. Two electrodes that served as electrical contacts were fabricated by using the indium microsoldering method [42,43].
[41] G. H. Han, N. J. Kybert, C. H. Naylor, B. S. Lee, J. L. Ping, J. H. Park, J. Kang, S. Y. Lee, Y. H. Lee, R. Agarwal, and A. T. C. Johnson, Nat. Commun. **6**, 6128 (2015).
[42] C. O. Girit and A. Zettl, Appl. Phys. Lett. **91**, 193512 (2007).
[43] V. Geringer, D. Subramaniam, A. K. Michel, B. Szafranek, D. Schall, A. Georgi, T. Mashoff, D. Neumaier, M. Liebmann, and M. Morgenstern, Appl. Phys. Lett. **96**, 082114 (2010).
[44] H. P. Komsa and A. V. Krasheninnikov, Phys. Rev. B **91**, 125304 (2015).
[45] The electrical characteristics of the devices as a function of gate bias were measured using an electrical characterization system (Keithley 4200-SCS, Keithley Instruments) under ambient conditions.
[46] See Supplemental Material at http://link.aps.org/supplemental/10.1103/PhysRevB.93.140409, which includes Refs. [47,48], for details on electrostatic doping concentrations and Fermi energy levels.

[47] N. R. Pradhan, D. Rhodes, Q. Zhang, S. Talapatra, M. Terrones, P. M. Ajayan, and L. Balicas, Appl. Phys. Lett. **102**, 123105 (2013).

[48] T. Cheiwchanchamnangij and W. R. L. Lambrecht, Phys. Rev. B **85**, 205302 (2012).

[49] PL spectra were measured by using a laboratory-made confocal microscope. We used a diode laser with a wavelength of 405 nm (filtered by a bandpass filter) and an objective lens with a numerical aperture of 0.6. The PL signals were recorded in a spectrometer and cooled charge-coupled device camera. The PL signal acquisition times range from 5 to 60 s for $P_{ex} = 0.5 - 500\,\mu$W and the signals are normalized by the acquisition time.

[50] V. Huard, R. T. Cox, K. Saminadayar, A. Arnoult, and S. Tatarenko, Phys. Rev. Lett. **84**, 187 (2000).

[51] W. Ossau, G. V. Astakhov, D. R. Yakovlev, W. Faschinger, V. P. Kochereshko, J. Puls, F. Henneberger, S. A. Crooker, Q. McCulloch, and A. Waag, in *Proceeding of the NATO Advanced Research Workshop on Optical Properties of 2D Systems with Interacting Electrons, St. Petersburg, Russia*, edited by W. J. Ossau and R. J. Suris, NATO Science, Series II: Mathematics, Physics, and Chemistry (Springer Science & Business Media, 2003), Vol. 119, p. 53.

[52] J. C. Kim, D. R. Wake, and J. P. Wolfe, Phys. Rev. B **50**, 15099 (1994).